Textile & Leather Review

ISSN 2623-6281 | www.tlr-journal.com | 10.31881/TLR

Phase-shifting algorithm for suppression of random intensity errors in measurement of silicon wafer surface shape

Bohang Zhong, Huaian Yi, Fuqing Miao

How to cite: Zhong B, Yi H, Miao F. Phase-shifting algorithm for suppression of random intensity errors in measurement of silicon wafer surface shape. Textile & Leather Review. 2026; 9:4477-4496. https://doi.org/10.31881/TLR.2026.4477

How to link: https://doi.org/10.31881/TLR.2026.4477

Published: 27 April 2026

Phase-shifting algorithm for suppression of random intensity errors in measurement of silicon wafer surface shape

Bohang Zhong[1,2], Huaian Yi[1,2], Fuqing Miao[1,2*]

[1]Guilin University of Technology, Guilin 541004, Guangxi, China

[2]Key Laboratory of Advanced Manufacturing and Automation Technology, College of Mechanical and Control Engineering, Guilin University of Technology, Guilin 541006, Guangxi, China

*15247602709@163.com

Article

https://doi.org/10.31881/TLR.2026.4477

Published 27 April 2026

ABSTRACT

This study investigates how random intensity variations affect phase-shifting methods for high-precision three-dimensional surface-topography reconstruction in precision interferometric measurement, with potential relevance to fibrous materials. To address this issue, a 9N-8 scheme was constructed based on characteristic polynomial theory by combining a newly designed polynomial-shaped window and a discrete Fourier transform component. The sensitivity of the proposed approach to stochastic intensity fluctuations was evaluated, and the corresponding root-sum-square (RSS) error was calculated and compared with those of standard phase-shifting methods. The proposed method was then applied in a wavelength-tuned Fizeau interferometer for surface-topography measurements of optical samples. Experimental results indicate that the 9N-8 approach achieves the lowest RMS and random-intensity errors among the compared techniques, demonstrating strong robustness against both coupling effects and stochastic intensity perturbations. Although the present validation was conducted on standard optical components, the proposed framework may provide methodological support for future interferometric measurement of fibrous materials, where scattering, reflectivity variation, and curved surface geometry introduce additional challenges.

KEYWORDS

interferometry, tunable-wavelength interferometry, surface shape, random intensity error, fibrous-material measurement

INTRODUCTION

Accurate characterization of optical thickness and surface topography is essential in precision manufacturing, particularly for components requiring strict geometric control. In addition, fibrous materials such as textile fibers and yarn assemblies present additional optical challenges, including scattering, reflectivity variation,

and curved surface geometry. Therefore, the development of robust high-accuracy surface-metrology methods is important not only in precision engineering but also for the potential extension of interferometric techniques to textile-related applications.

Several techniques have been proposed for optical metrology [1-5]. Tunable-wavelength interferometry has been adopted as an effective method to obtain surface profiles of silicon wafers [6]. In this setup, the phase is incrementally adjusted across the reference and sample surfaces, and the resulting fringe patterns are captured at each step. These collected data are then analyzed to reconstruct the complete phase distribution [7].

For reflective samples, error sources are not limited to harmonic distortion and phase-shift inaccuracy [8]. Random intensity fluctuations must also be considered, since unstable driving current may cause laser-power variation and thereby introduce intensity noise into the interferometric signal [9]. This issue directly affects phase retrieval and becomes more critical under high-precision measurement conditions.

To improve robustness against systematic errors, a variety of phase-shifting methods have been introduced [10-25]. Early and later representative methods differ in their abilities to suppress phase-shift miscalibration, coupling errors, harmonic effects, and nonlinear distortion. Algorithms derived from extended averaging, data-sampling windows, characteristic polynomial theory, and Fourier representation have all contributed to error compensation in interferometric measurement [13-25]. In particular, characteristic-polynomial-based methods have provided an important route for simultaneously addressing multiple error sources, while later improved schemes further reduced standard deviation and enhanced reconstruction quality [16, 19, 21-27].

Interferometric metrology has also advanced rapidly in recent years, promoting more accurate wafer-surface measurement. Thin-film-interference-based systems, stitching-based optical configurations, multiscale frequency-extraction methods, and parameter time-domain estimation strategies have all been reported to improve measurement capability [28-31]. Nevertheless, most of these studies did not explicitly address random intensity fluctuations. Although Kim's 7N-6 algorithm [32] examined susceptibility to random intensity errors, increasingly stringent precision requirements still leave room for further improvement. A phase-shifting algorithm with stronger comprehensive compensation capability is therefore still needed.

To meet this requirement, a 9N−8 phase-shifting scheme is proposed in this study by integrating a polynomial window with a Fourier-transform-based term. The method mitigates random intensity errors while improving phase-retrieval robustness in precision interferometric measurement. In the present study, it was validated

on reflective surfaces to assess its performance under controlled conditions. Its performance was further evaluated through frequency-domain analysis and comparison with conventional phase-shifting schemes, showing improved phase accuracy and enhanced overall error-suppression capability. The potential extension of the proposed framework to fibrous-material measurement is discussed as a future research direction.

Derivation of susceptibility formula

During laser Fizeau interferometry, the optical intensity measured by the CCD camera is represented mathematically as

$$I(\alpha_k) = A_0 + \sum_{m=1}^{\infty} A_m \cos(\phi_m - m\alpha_k). \tag{1}$$

In this formulation, α_k represents the phase-shift parameter, A_0 corresponds to the DC term, and each A_m along with its associated ϕ_m specifies the amplitude and phase of the m-th harmonic component.

The general expression of an M-sample algorithm can be written as

$$\phi = \arctan \frac{\sum_{k=1}^{M} b_k I_k}{\sum_{k=1}^{M} a_k I_k}. \tag{2}$$

In this formulation, ϕ represents the target phase. At each sampling step k , the coefficients a_k and b_k define the sampling amplitudes, while I_k indicates the measured intensity ($I_k = I(\alpha_k)$). The random intensity variation $\delta I(\alpha_k)$ is considered independent across different samples [33]. Based on these definitions, the associated phase variation $\delta\phi$ [34] may be expressed as

$$\begin{aligned}\delta\phi &= \delta\left[\arctan\frac{\sum_{k=1}^{M} b_k I_k}{\sum_{k=1}^{M} a_k I_k}\right] \\ &= \sum_{k=1}^{M}\frac{\delta I_k}{1+\left[\sum_{j=1}^{M} b_j I_j / \sum_{j=1}^{M} a_j I_j\right]^2}\frac{\partial}{\partial I_k}\left(\frac{\sum_{k=1}^{M} b_k I_k}{\sum_{k=1}^{M} a_k I_k}\right) \\ &\simeq -\sum_{k=1}^{M}\left(\frac{\delta I_k}{A_1}\right)(b_k\cos\phi_1 - a_k\sin\phi_1) \\ &= -\sum_{k=1}^{M}\left(\frac{\delta I_k}{A_1}\right)\sqrt{a_k^2+b_k^2}\cos(\phi_1+\beta_k)\end{aligned} \tag{3}$$

In this context, A_1 is the main amplitude of the signal. If the systematic error is sufficiently small relative to π radians, the two expressions in Eq. (2) may be approximated using the sine and cosine terms corresponding to the object phase ϕ_1 .

(4)

$$\sum_{k=1}^{M} b_k I_k \approx A_1\sin\phi_1 \tag{5}$$

Because the random intensity errors of different samples are statistically independent [33], the variance of the phase error $\delta\phi$ can be written as

$$\delta\phi^2 = \langle\Delta\phi^2\rangle = \frac{1}{A_1^2}\sum_{k=1}^{M}\langle\delta I_k^2\rangle(a_k^2+b_k^2)\cos^2(\phi_1+\beta_k). \tag{6}$$

The angle brackets denote statistical averaging, and the variance is dependent on the object phase ϕ_1 . If this dependence on ϕ_1 is neglected and averaging is performed over ϕ_1 , the mean RMS error $\delta\phi$ can be written as

$$\delta\phi = \frac{1}{\sqrt{2}}\frac{\delta I}{A_1}\sqrt{\sum_{k=1}^{M}(a_k^2+b_k^2)} \tag{7}$$

In this analysis, the random intensity variation is considered to have a uniform standard deviation, represented by δI for each sample. Based on Eq. (7), the algorithm's susceptibility is calculated using the root-sum-square (RSS) method as follows:

$$RSS = \sqrt{\sum_{k=1}^{M}(a_k^2 + b_k^2)}. \tag{8}$$

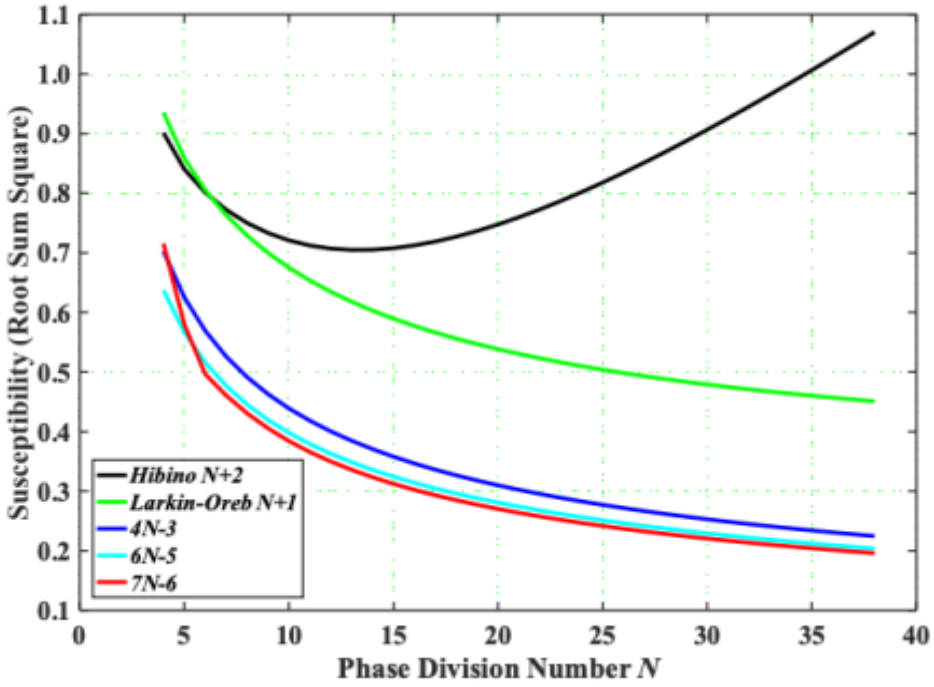

Figure 1: Comparison of susceptibility values for multiple traditional algorithms

Figure. 1 shows the sensitivity values of several conventional phase-shifting algorithms, including Hibino N +2 [34], Larkin–Oreb N +1 [13], and Kim's 4 N −3 [23], 6 N −5 [25], and 7 N −6 [32] schemes. For the Hibino N +2 algorithm, the sensitivity first declines at small phase division numbers N and then rises as N increases. To mitigate the effect of the m -th harmonic, the phase division number should satisfy N > m + 2 [35,36]. The Larkin–Oreb N +1 algorithm achieves a minimum RMS metric when harmonic components are effectively suppressed; however, it does not address coupling errors, which limits its suitability for highly reflective surfaces. In comparison, Kim's 4 N −3, 6 N −5, and 7 N −6 algorithms exhibit a gradual decrease in RMS as N grows. Following this rationale, a lower-susceptibility phase-shifting scheme was further pursued in this

study. The detailed construction of the proposed 9 N −8 algorithm, based on characteristic polynomial theory and a polynomial-shaped window, is presented in Section 2.2.

Derivation of 9 N −8 algorithm

Characteristic polynomial theory

Surrel [16] introduced an approach to derive algorithms designed to meet measurement objectives while remaining robust against both harmonic disturbances and phase-shift miscalibration. This framework incorporates a triangular-shaped window combined with a discrete Fourier transform and is formulated as follows:

$$P(x) = \sum_{k=0}^{M-1} (a_k + ib_k)x^k. \tag{9}$$

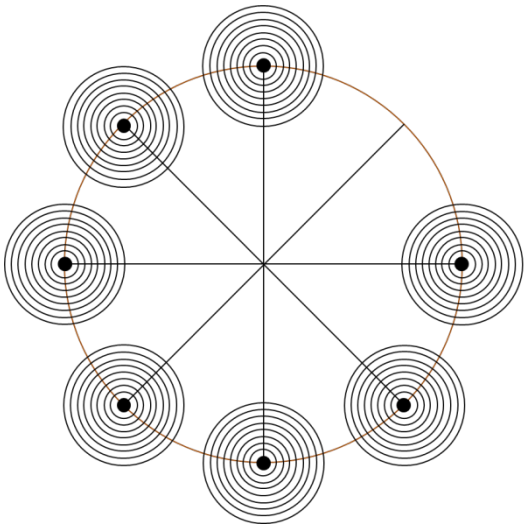

Figure 2: Root distribution in the characteristic polynomial of the 9N−8 scheme (N = 8)

In this formulation, i is the imaginary unit, x is defined as exp($i\alpha$), and $\alpha = 2\pi/N$. According to Surrel's theory, the sensitivity of the algorithm to harmonic distortion and phase-shift error depends on the number and distribution of roots in the characteristic polynomial. In Bruning's synchronous detection [36], the complex polynomial contains only one root. To improve resistance to phase-shift error and coupling effects, Surrel proposed the 2 N −1 algorithm by assigning double roots in the characteristic polynomial [16]. For accurate measurement of highly reflective specimens such as silicon wafers, both systematic errors, including phase-shift and harmonic effects, and random intensity fluctuations must be suppressed. On this basis, the present study constructs the 9 N −8 algorithm by introducing nine multiple roots into the characteristic polynomial, so

that phase-shift nonlinearity up to the seventh order and coupling errors can be effectively compensated. To construct the corresponding polynomial-shaped window, a set of design constraints was imposed, including symmetry with respect to the central sampling position, zero-value conditions at selected frequency points, and zero-derivative conditions up to the seventh order for suppressing sidelobes, harmonic effects, and coupling-related errors. The coefficients of the window function were obtained using symbolic computation to satisfy these constraints simultaneously. The constructed polynomial-shaped window was thus obtained through a constraint-based formulation under the above design requirements, rather than being introduced as an ad hoc symbolic expression. The corresponding sampling amplitudes of the 9 N −8 algorithm are given below:

$$a_k = \frac{2}{N} w_k \cos \frac{2\pi}{N} \left(k - \frac{9N-7}{2} \right), \tag{10}$$

$$b_k = \frac{2}{N} w_k \sin \frac{2\pi}{N} \left(k - \frac{9N-7}{2} \right). \tag{11}$$

Here, w_k represents the polynomial-shaped window introduced in the Appendix. The constructed window is designed to be symmetric around $k = (9N-8)/2$, and its resulting profile is shown in Figure. 3.

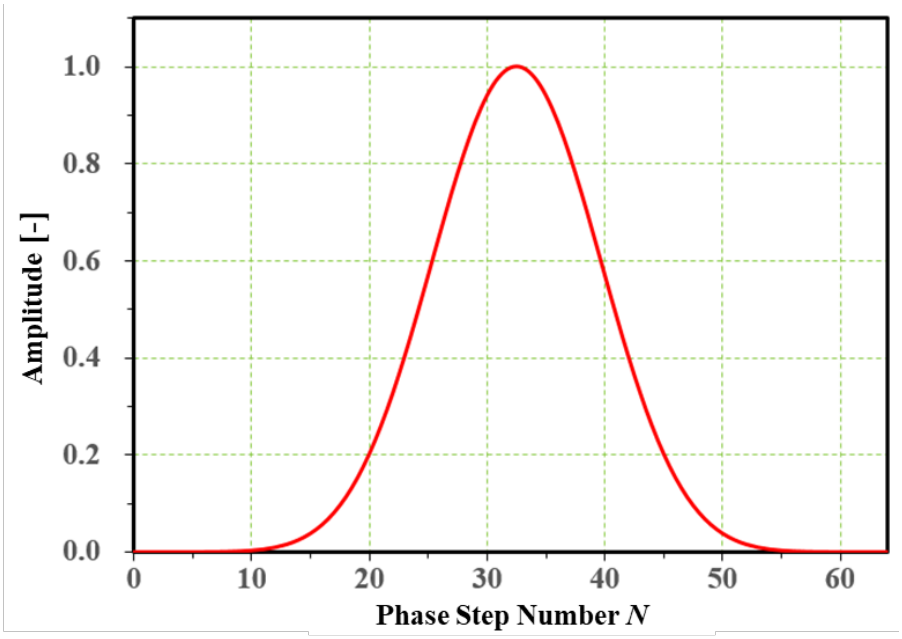

Figure 3: Profile of the polynomial-shaped window function

Fourier-domain Expression of the 9N-8 Algorithm

To analyze the characteristics of the phase-shifting method, the sampling functions are expressed in the Fourier domain [13, 38]. Under this formulation, the numerator $f_1(\alpha)$ and denominator $f_2(\alpha)$ are given by

$$f_1(\alpha) = \sum_{k=1}^{M} b_k \delta(\alpha - \alpha_k), \tag{12}$$

$$f_2(\alpha) = \sum_{k=1}^{M} a_k \delta(\alpha - \alpha_k). \tag{13}$$

Here $\delta(\alpha)$ represents the Dirac delta function, and the corresponding Fourier-domain expressions are written as follows:

$$F_1(v) = \sum_{k=1}^{M} b_k \exp(-i\alpha_k v), \tag{14}$$

$$F_2(v) = \sum_{k=1}^{M} a_k \exp(-i\alpha_k v). \tag{15}$$

In these expressions, i represents the imaginary unit, and ν corresponds to frequency. According to [37], F_1 is entirely imaginary, whereas F_2 is entirely real. This characteristic ensures that the algorithm satisfies both symmetry and asymmetry requirements. The properties of the constructed window function, including symmetry and the prescribed zero-derivative conditions at the specified frequency points, were further verified numerically to ensure consistency with the design requirements.

The sampling functions for the 9 N −8 algorithm are illustrated in Figure. 4. As reported in Table 1, the 9 N −8 scheme achieves a sidelobe level of 0.0008%, outperforming Surrel's 2 N −1 algorithm (5.5883%), Hanayama's 2 N −1 algorithm (1.4339%), the 4 N −3 algorithm (0.256%), the 6 N −5 algorithm (0.012%), and the 7 N −6 algorithm (0.003%). These results confirm the superior side-lobe reduction capability of the 9 N −8 algorithm among the methods compared.

For this scheme, the sampling functions are designed to have zero first-order derivatives at the relative frequency ν =1, satisfying the condition for maximum fringe contrast [24]. Zero-gradient points are also observed

at ν =0 and at ν =2,3,…,7, enabling compensation for bias modulation and coupling errors. The derivatives are further constrained to remain zero up to the seventh order, ensuring that coupling errors can be effectively mitigated to the order $o(A_m\epsilon_7)$.

Table 1. Comparison of sidelobe and compensation ability between algorithms

Algorithms	Sidelobe (%)	Phase-shift error	Coupling error
Surrel's 2 N −1	5.5883	$O(\epsilon_0)$	$O(A_m\epsilon_0)$
Hanayama's 2 N - 1	1.4339	$O(\epsilon_0)$	$O(A_m\epsilon_0)$
4 N −3	0.256	$O(\epsilon_2)$	$O(A_m\epsilon_2)$
6 N −5	0.012	$O(\epsilon_4)$	$O(A_m\epsilon_4)$
7 N −6	0.003	$O(\epsilon_5)$	$O(A_m\epsilon_5)$
9 N −8	0.0008	$O(\epsilon_7)$	$O(A_m\epsilon_7)$

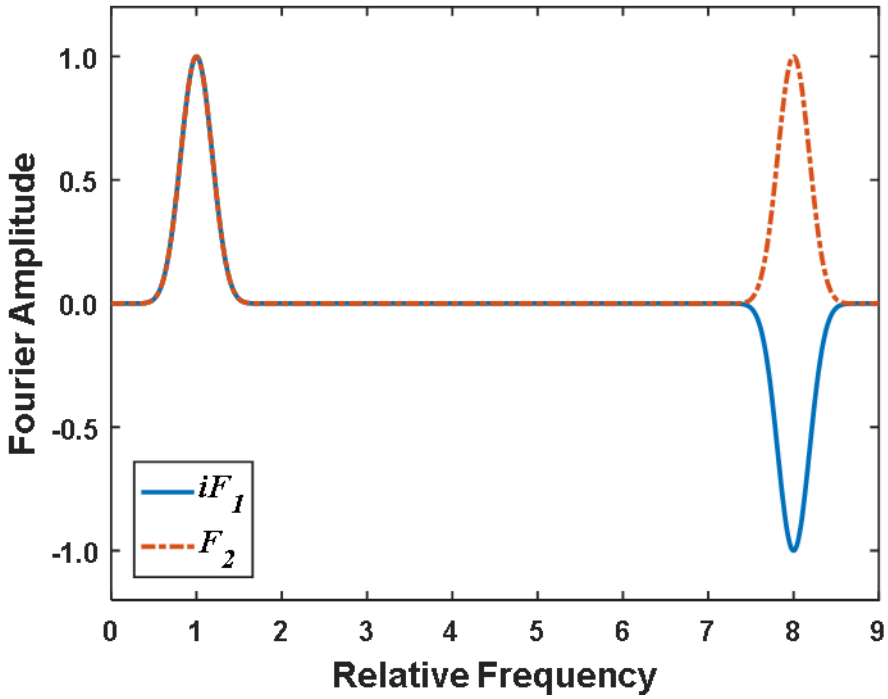

Figure 4: Sampling profiles of the 9N-8 algorithm (N = 8)

Error analysis

De Groot [39] derived an analytical expression to evaluate the suppression of phase errors caused by harmonic components and phase-shift miscalibration. In this framework, the impact of phase-shift miscalibration on measurement errors is assessed using the RMS value, calculated as:

$$\sigma_m = \frac{1}{2\sqrt{2}} \left| \frac{iF_1(v)}{F_2(v)} - 1 \right|. \tag{16}$$

Here, i denotes the imaginary unit, while $F_1(v)$ and $F_2(v)$ are derived from Eq. (14) and Eq. (15), respectively. The RMS value corresponding to the coupling error can be written as

$$\sigma_c = \frac{1}{2} \sum_{m=2}^{\infty} \frac{\gamma_m}{\gamma_1} \sqrt{\left[\frac{iF_1(mv)}{iF_1(v)} \right]^2 + \left[\frac{F_2(mv)}{F_2(v)} \right]^2}, \tag{17}$$

Here, γ_m represents the fringe contrast corresponding to the m -th harmonic. This parameter can be estimated using the reflectivities of both the sample and reference surfaces. Accordingly, the resulting RMS error is calculated as:

$$\sigma = \sqrt{\sigma_m^2 + \sigma_c^2}. \tag{18}$$

Figure. 5 illustrates the RMS behavior under reflectivity conditions of approximately 4% for the reference surface and 30% for the sample surface. Among the compared methods, the 9 N −8 algorithm achieves the lowest RMS value under the present simulation conditions. Even when the phase-shift error is close to 30%, the method continues to exhibit low RMS levels, indicating reliable performance for the characterization of highly reflective surfaces.

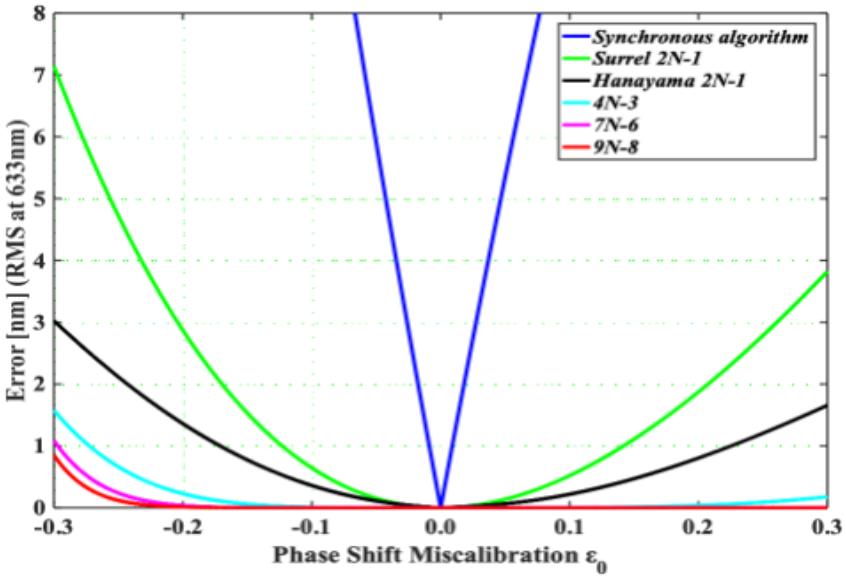

Figure 5: Root-mean-square (RMS) metric versus phase-shift deviations for surfaces with reflectivities of approximately 4% and 30%

Susceptibility of new algorithm

Fig. 6 shows a comparison of sensitivity values between the 9 N −8 method and several standard phase-shifting algorithms. The data indicate that the sensitivity of all evaluated algorithms decreases as the phase division number N increases. For $N = 4$, the 9 N −8 approach exhibits higher sensitivity than the 4 N −3, 6 N −5, and 7 N −6 schemes. In practical applications, where both optical thickness and surface profile need to be measured simultaneously, the phase division number is typically chosen above 8 [17, 23]. Under these conditions, the 9 N −8 algorithm demonstrates lower sensitivity compared with the conventional 4 N −3, 6 N −5, and 7 N −6 methods when $N > 8$.

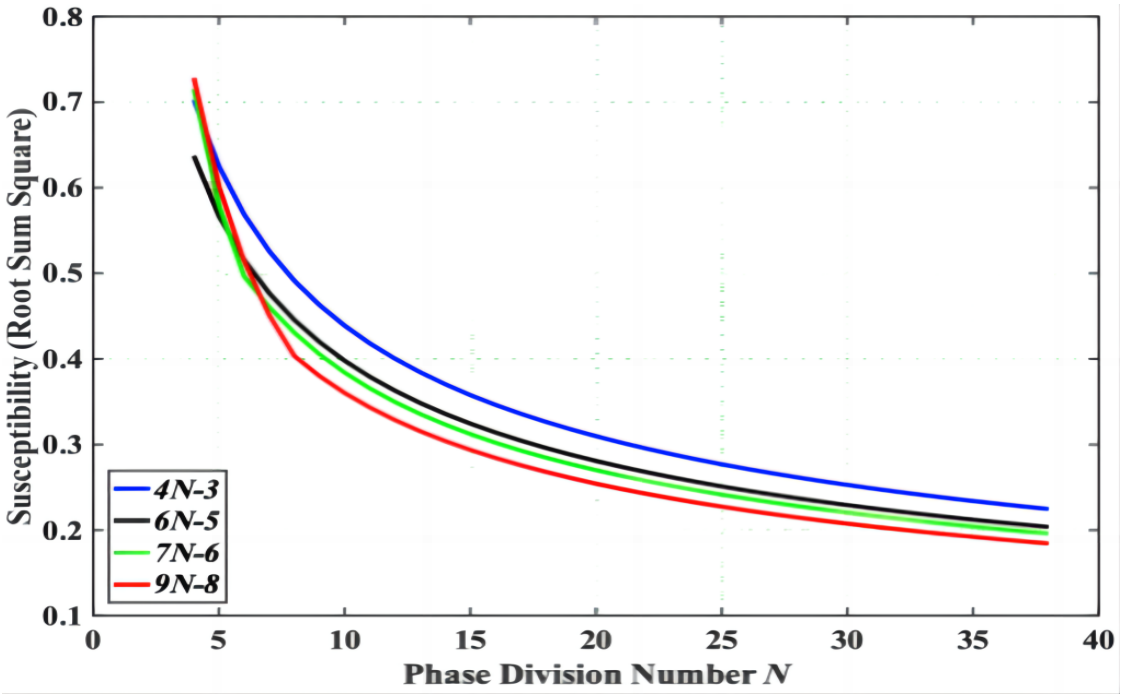

Figure 6: The susceptibility of 4N-3, 6N-5, 7N-6, and 9N-8 algorithms

RESULTS

Wavelength-Tuned Fizeau Interferometry

Figure. 7 illustrates the experimental setup of the wavelength-tuned Fizeau interferometer. This system was used for surface-topography measurement of a 4-inch silicon wafer under controlled laboratory conditions.

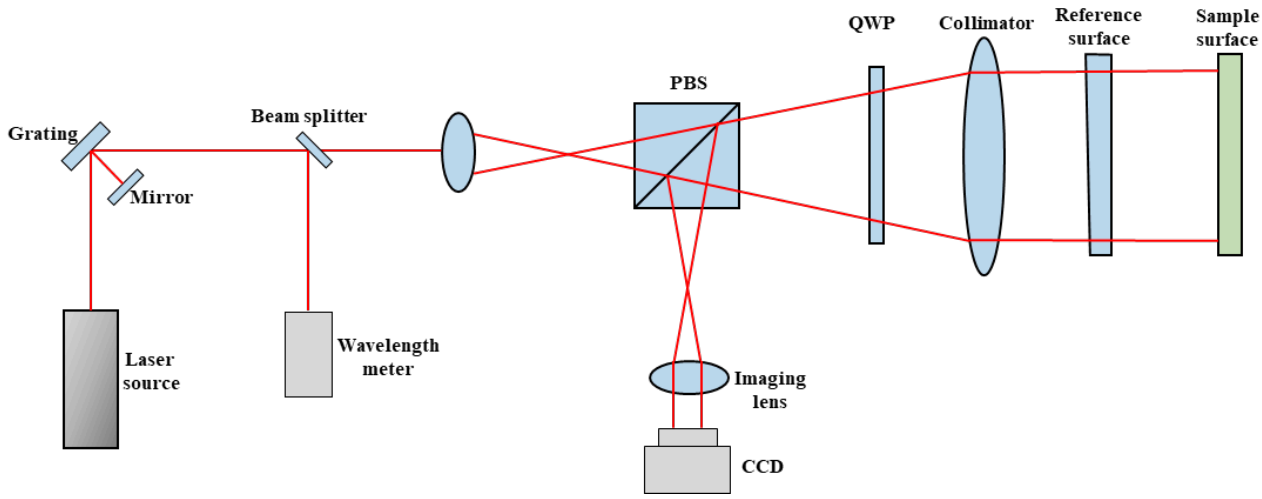

Figure 7: Optical arrangement of the wavelength-tuning Fizeau interferometer. PBS: Polarization Beam Splitter; HWP: Half-Wave Plate; QWP: Quarter-Wave Plate

Illumination was provided by a Littman-type tunable diode laser (NewFocus TLB-6804) with mode-hop-free fine-frequency tuning exceeding 120 GHz. Linear wavelength tuning from 632.5 to 640 nm was achieved using a Picomotor actuator (Newport). The emitted beam was then split into two optical paths, one directed to a wavelength meter (Anritsu MF9630A) with measurement uncertainty of approximately 10^{-7} , and the other guided into the Fizeau interferometer.

The collimated beams illuminated both the reference and silicon-wafer sample surfaces. Reflected beams then passed sequentially through a quarter-wave plate (QWP) and a polarizing beam splitter (PBS), producing interferograms at the detection plane. These interferograms were captured using a CCD camera (DMK 33G445, The Imaging Source) and digitized with the associated ADC (DFG/USB2pro, The Imaging Source). For preparation, the sample wafer was fixed on a mechanical stage with a 10 mm air gap from the reference surface. All measurements were conducted under controlled laboratory conditions at 20.5 ± 0.1 °C.

To remove its internal temperature gradient, a BK7 plate (SCHOTT; diameter: 10 cm; thickness: 5 mm; refractive index: 1.515 at 633 nm) was acclimatized in the laboratory for one day prior to measurement. Subsequently, the BK7 plate was characterized using the proposed 9N-8 algorithm integrated with the wavelength-tuning Fizeau interferometer. It should be noted that the present experimental validation was conducted on **optical samples**, including a silicon wafer and a BK7 plate, rather than fibrous materials. This design was adopted to isolate the influence of random intensity fluctuations and to evaluate the intrinsic error-suppression capability of the proposed algorithm under controlled interferometric conditions. Compared with

textile fibers and yarn assemblies, such optical samples exhibit more stable reflectivity and weaker scattering, and therefore provide suitable benchmark objects for methodological verification. The applicability of the proposed framework to textile-related measurements will require further investigation under conditions involving scattering, non-uniform reflectance, and curved microgeometry.

Table 2. Technical parameters of DMK 33G445

Items	Technical Parameters
Dynamic range	12 bits
Resolution	1,280×960 pixels
Frame rate	30 fps
Pixel size	Vertical/horizontal: 3.75 μ m
Sensor	SONY ICX 445ALA
Shutter	10 μ s ~ 30 s
Gain	0 dB ~ 30.39 dB

Experimental results

The phase distribution of the silicon wafer was retrieved using the proposed method and subsequently unwrapped. Figure. 8 displays the overall wafer configuration. Over a period of 4 days, 20 consecutive experiments were carried out. The measured wafer surface reached a maximum PV value of 405 nm. Only slight ripple features were visible in the reconstructed results, indicating that the 9 N −8 algorithm provides effective suppression of phase-retrieval error under the present experimental conditions.

Because of laboratory disturbances, including floor vibration and temperature fluctuation, the measurement repeatability was 2.405 nm. Under more stable experimental conditions, these effects could be further reduced by using a laser source with better stability. The uncertainty of the surface-topography measurement was around $\lambda/30$, or roughly 21 nm, while the total uncertainty of the surface-topography measurement was estimated at about 23 nm.

The remaining algorithms were also tested experimentally, and the resulting surface topographies were almost identical. Table 3 summarizes the standard-deviation differences among the compared algorithms. Among them, the 9 N −8 algorithm achieved the lowest standard deviation under the present test conditions, indicating the strongest overall suppression of coupling-related errors among the compared methods. By comparison, Surrel's 2 N −1 algorithm exhibited the largest standard deviation, suggesting the weakest compensation capability for phase-shift and coupling-related errors.

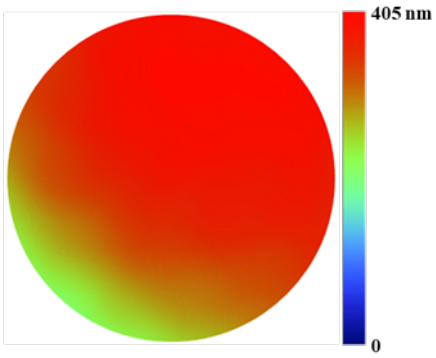

Figure 8: Surface shape of silicon wafer

Table 3. Comparison of standard deviation for different algorithms

Algorithm	Std.Deviation (nm)
Surrel's 2 N - 1	8.93
Hanayama's 2 N - 1	8.19
Kim's 4 N - 3	4.14
6 N - 5	3.11
7 N - 6	2.50
9 N - 8	2.40

CONCLUSIONS

A 9N-8 phase-shifting algorithm was developed in this study to achieve strong sidelobe suppression together with effective compensation for bias modulation and coupling errors, thereby improving the robustness of phase retrieval in precision interferometric measurement. The proposed method provides a reliable framework for high-precision surface-topography measurement of highly optical samples.

An important but often insufficiently considered error source arises from the interaction between harmonic components and phase-shift miscalibration [39]. For wavelength-tuned Fizeau interferometry, phase-shift errors amplify the contribution of higher-order harmonics and consequently impair measurement precision. The proposed method was evaluated through both theoretical analysis and experimental verification.

Root-mean-square (RMS) errors were evaluated for Surrel's 2 N −1, Hanayama's 2 N −1, Kim's 4 N −3, 6 N −5, and 7 N −6 methods, as well as the proposed 9 N −8 algorithm, under reference- and sample-surface reflectivities of 4% and 30%, respectively. Among the compared methods, the 9 N −8 algorithm achieved the lowest RMS value under the present conditions, indicating better performance in measuring the surface topography of silicon wafers.

Furthermore, an analytical framework was developed to examine the response of phase-shifting algorithms to random intensity variations. The performance of the proposed 9 N −8 method was compared with Kim's 4 N −3, 6 N −5, and 7 N −6 schemes. The results indicate that the 9 N −8 algorithm maintains strong robustness against both coupling effects and stochastic intensity perturbations. Although the present validation was limited to standard optical samples, the proposed framework may provide methodological support for future interferometric measurement of fibrous materials, where scattering, reflectivity variation, and curved surface geometry require further investigation.

Author Contributions

Conceptualization –Bohang Zhong, Huaian Yi and Fuqing Miao; methodology – Bohang Zhong, Huaian Yi and Fuqing Miao; investigation – Bohang Zhong, Huaian Yi and Fuqing Miao; writing-original draft preparation – Bohang Zhong, Huaian Yi and Fuqing Miao. All authors have read and agreed to the published version of the manuscript.

Conflicts of Interest

The authors declare no conflict of interest.

Funding

This research was supported by Guangxi Science and Technology Program (GUIKEAD23026238), the Scientific Research Foundation of Guilin University of Technology (RD2100001761), and the Project for Enhancing Young and Middle-aged Teacher's Research Basis Ability in Colleges of Guangxi (2023KY0267).

Acknowledgements

Not applicable.

REFERENCES

[1] Malacara D. Optical shop testing. Third Ed. John Wiley & Sons, Inc. Hoboken, New Jersey, USA: John Wiley & Sons, Inc.; 2007. doi: 10.1002/9780470135976

[2] Ma S, Quan C, Zhu R et al. Investigation of phase error correction for digital sinusoidal phase-shifting fringe projection profilometry. Opt. & Laser in Eng. 2012, 50, 1107-1118. doi: 10.1016/j.optlaseng.2012.01.021

[3] Huang Y, Ma J, Zhu R et al. Absolute measurement of optical flat surface shape based on the conjugate differential method. Opt. Express 2015, 23, 29687-29697. doi: 10.1364/OE.23.029687

[4] Yoshizawa T. Handbook of Optical Metrology: Principles and Applications. New York, USA: Taylor & Francis Group; 2017. doi: 10.1201/b18328

[5] Lyu HY, Huang YS, Sheng B et al. Absolute optical flatness testing by surface shape reconstruction using Zernike polynomials. Opt. Eng. 2018, 57, 094103. doi: 10.1117/1.OE.57.9.094103

[6] Malacara D, Servin M, Malacara Z. Interferogram analysis for optical testing. New York, USA: Taylor & Francis Group; 2005. doi: 10.1201/9781420027273

[7] Creath K. Phase-measurement interferometry techniques. Progress in Optics, Elsevier Science Publishers B.V. North-Holland, 1988. doi: 10.1016/S0079-6638(08)70178-1

[8] Kim Y, Sugita N, Mitsuishi M. Measurement of highly reflective surface shape using wavelength tuning Fizeau interferometer and polynomial window function. Precision Eng. 2016, 45, 187-194. doi: 10.1016/j.precisioneng.2016.02.011

[9] Ishii Y, Chen J, Murata K. Digital phase-measuring interferometry with a tunable laser diode. Opt. Lett. 1987, 12, 233-235. doi: 10.1364/OL.12.000233

[10] Carre P. Installation et utilisation du comparateur photoelectrique et interferential du Bureau International des Poids et Mesures. Metrologia. 1966, 2, 13-23. doi: 10.1088/0026-1394/2/1/005

[11] Schwider J, Burow R, Elssner KE, Grzanna J, Spolaczyk R, Merkel K. Digital wavefront measuring interferometry: Some systematic error sources. Appl. Opt. 1983, 22, 3421-3432. doi: 10.1364/AO.22.003421

[12] Hariharan P. Digital phase-stepping interferometry: effects of multiply reflected beams. Appl. Opt. 1987, 26, 2506-2507. doi: 10.1364/AO.26.002506

[13] Larkin KG, Oreb BF. Design and assessment of symmetrical phase-shifting algorithms. J. Opt. Soc. Am. A. 1992, 9, 1740-1748. doi: 10.1364/JOSAA.9.001740

[14] Schmit J, Creath K. Extended averaging technique for derivation of error-compensating algorithms in phase-shifting interferometry. Appl. Opt. 1995, 34, 3610-3619. doi: 10.1364/AO.34.003610

[15] De Groot P. Derivation of algorithms for phase-shifting interferometry using the concept of a data-sampling window. Appl. Opt. 1995, 34, 4723-4730. doi: 10.1364/AO.34.004723

[16] Surrel Y. Design of algorithms for measurements by the use of phase stepping. Appl. Opt. 1996, 35, 51-60. doi: 10.1364/AO.35.000051

[17] De Groot P. Measurement of transparent plates with wavelength-tuned phase-shifting interferometry. Appl. Opt. 2000, 39, 2658-2663. doi: 10.1364/AO.39.002658

[18] Hariharan P. Optical interferometry. Academic Press, 2003. doi: 10.1016/B978-012311630-7/50002-2

[19] Hibino K, Oreb BF, Fairman PS. Wavelength-scanning interferometry of a transparent parallel plate with refractive-index dispersion. Appl. Opt. 2003, 42, 3888-3895. doi: 10.1364/AO.42.003888

[20] Hanayama R, Hibino K, Warisawa S, Mitsuishi M. Phase measurement algorithm in wavelength scanned Fizeau interferometer. Opt. Review 2004, 11, 337-343. doi: 10.1007/s10043-004-0337-3

[21] Hibino K, Oreb BF, Fairman PS, Burke J. Simultaneous measurement of surface shape and variation in optical thickness of a transparent parallel plate in wavelength scanning Fizeau interferometer. Appl. Opt. 2004, 43, 1241-1249. doi: 10.1364/AO.43.001241

[22] Kakue T, Moritani Y, Ito K, Shimozato Y, Awatsuji Y, Nishio K, Ura S, Kubota T, Matoba O. Image quality improvement of parallel four-step phase-shifting digital holography by using the algorithm of parallel two-step phase-shifting digital holography. Opt. Express 2010, 18, 9555-9560. doi: 10.1364/OE.18.009555

[23] Kim Y, Hibino K, Hanayama R, Sugita N, Mitsuishi M. Multiple-surface interferometry of highly reflective wafer by wavelength tuning. Opt. Express 2014, 22, 21145-21156. doi: 10.1364/OE.22.021145

[24] Kim Y, Hibino K, Sugita N, Mitsuishi M. Design of phase shifting algorithm: fringe contrast maximum. Opt. Express 2014, 22, 18203-18213. doi: 10.1364/OE.22.018203

[25] Kim Y, Hibino K, Sugita N et al. Simultaneous measurement of surface shape and optical thickness using wavelength tuning and a polynomial window function. Opt. Express. 2015, 23, 32869-32880. doi: 10.1364/OE.23.032869

[26] Miao F, Ahn S, Moon YH et al. Surface profilometry of silicon wafers using wavelength-tuned phase-shifting interferometry. J. Mech. Sci. Technol. 2019, 33, 5327-5335. doi: 10.1007/s12206-019-1025-3

[27] Miao F, Ahn S, Kim Y. Precise Measurement of the Surface Shape of Silicon Wafer by Using a New Phase-Shifting Algorithm and Wavelength-Tuning Interferometer. Appl. Sci. 2020, 10, 3250. doi: 10.3390/app10093250

[28] Ye R, Zeng J, Zhang H, Su Y, Li H. Rapid Full-Field Surface Topography Measurement of Large-Scale Wafers Using Interferometric Imaging. Photonics 2025, 12, 835. doi: 10.3390/photonics12090835

[29] Ivanov-Kurtev K, Trujillo-Sevilla JM, Rodríguez-Ramos JM. Stitching-Based Resolution Enhancement in Wavefront Phase Measurement of Silicon Wafer Surfaces. Appl. Sci. 2025, 15, 1019. doi: 10.3390/app15031019

[30] Ding YF, Lu Q, Liu SJ et al. Surface profile measurement of transparent parallel plates by multi-scale analysis phase-shifting interferometry (MAPSI). Optics and Laser in Eng. 2024, 181, 108432. doi: 10.1016/j.optlaseng.2024.108432

[31] Zhou YH, Yu YJ, Zhao ZL et al. Wavelength Phase-Shifting Interferometry for Simultaneous Profiling of Surface and Thickness Variation of Blank Mask. Laser & Optoelectronics Progress. 2025, 62, 0512001. doi: 10.3788/LOP242196

[32] Kim Y, Hibino K, Sugita N et al. Interferometric measurement of surface shape by wavelength tuning suppressing random intensity error. Appl. Opt. 2016, 55, 6464-6470. doi: 10.1364/AO.55.006464

[33] Brophy CP. Effect of intensity error correlation on the computed phase of phase-shifting interferometry. J. Opt. Soc. Am. A 1990, 7, 537-541. doi: 10.1364/JOSAA.7.000537

[34] Hibino K. Susceptibility of systematic error-compensating algorithms to random noise in phase-shifting interferometry. Appl. Opt. 1997, 36, 2084-2093. doi: 10.1364/AO.36.002084

[35] Hibino K, Oreb BF, Farrant DI, Larkin KG. Phase-shifting algorithms for nonlinear and spatially nonuniform phase shift. J. Opt. Soc. Am. A 1997, 14, 918-930. doi: 10.1364/JOSAA.14.000918

[36] Bruning JH, Herriott DR, Gallagher JE, Rosenfeld DP, White AD, Brangaccio DJ. Digital wavefront measuring interferometer for testing optical surfaces and lenses. Appl. Opt. 1974, 13, 2693-2703. doi: 10.1364/AO.13.002693

[37] Hibino K, Oreb BF, Farrant DI, Larkin KG. Phase-shifting for nonsinusoidal waveforms with phase-shift errors. J. Opt. Soc. Am. A 1995, 12, 761-768. doi: 10.1364/JOSAA.12.000761

[38] Freischlad K, Koliopoulos CL. Fourier description of digital phase-measuring interferometry. J. Opt. Soc. Am. A 1990, 7, 542-551. doi: 10.1364/JOSAA.7.000542

[39] De Groot P. Correlated errors in phase-shifting laser Fizeau interferometry. Appl. Opt. 2014, 53, 4334-4342. doi: 10.1364/AO.53.004334

[40] Liu K, Littman MG. Novel geometry for single-mode scanning of tunable lasers. Opt. Lett. 1981, 6, 117-118. doi: 10.1364/OL.6.000117

APPENDIX A

The polynomial expressions listed in this appendix were generated using symbolic computation under the symmetry, zero-value, and zero-derivative constraints described in Section 2.2.1.

1) $1 \le k \le N$

$$w_k = \frac{1}{40320}k(k+1)(k+2)(k+3)(k+4)(k+5)(k+6)(k+7)$$

2) $N+1 \le k \le 2N$

$$w_k = -\frac{1}{5040}k^8 + \left(\frac{1}{560}N - \frac{1}{180}\right)k^7 + \left(-\frac{1}{160}N^2 + \frac{1}{160}N - \frac{13}{360}\right)k^6 + \left(\frac{1}{80}N^3 - \frac{1}{160}N^2 + \frac{69}{160}N - \frac{7}{18}\right)k^5 + \left(-\frac{1}{64}N^4 + \frac{1}{32}N^3 - \frac{69}{64}N^2 + \frac{35}{16}N - \frac{967}{720}\right)k^4 + \left(\frac{1}{80}N^5 - \frac{7}{32}N^4 + \frac{23}{16}N^3 - \frac{35}{8}N^2 + \frac{976}{160}N - \frac{469}{180}\right)k^3 + \left(-\frac{1}{160}N^6 + \frac{21}{160}N^5 - \frac{69}{64}N^4 + \frac{35}{8}N^3 - \frac{2901}{320}N^2 + \frac{1407}{160}N - \frac{363}{140}\right)k^2 + \left(\frac{1}{560}N^7 - \frac{1}{160}N^6 + \frac{69}{160}N^5 - \frac{35}{16}N^4 + \frac{967}{160}N^3 - \frac{1407}{160}N^2 + \frac{3267}{560}N - 1\right)k + \left(-\frac{1}{4480}N^8 - \frac{1}{160}N^7 + \frac{23}{320}N^6 - \frac{7}{16}N^5 + \frac{967}{640}N^4 - \frac{496}{160}N^3 + \frac{3267}{1120}N^2 + \frac{9}{8}N\right)$$

3) $2N+1 \le k \le 3N$

$$w_k = \frac{1}{1440}k^8 + \left(-\frac{1}{80}N + \frac{7}{360}\right)k^7 + \left(\frac{3}{32}N^2 - \frac{49}{160}N + \frac{161}{720}\right)k^6 + \left(-\frac{31}{80}N^3 + \frac{63}{32}N^2 - \frac{483}{160}N + \frac{49}{36}\right)k^5 + \left(\frac{63}{64}N^4 - \frac{217}{32}N^3 + \frac{1035}{64}N^2 - \frac{245}{16}N + \frac{6769}{1440}\right)k^4 + \left(-\frac{127}{80}N^5 + \frac{441}{32}N^4 - \frac{713}{16}N^3 + \frac{525}{8}N^2 - \frac{6769}{160}N + \frac{3283}{360}\right)k^3 + \left(\frac{51}{32}N^6 - \frac{2667}{160}N^5 + \frac{4347}{64}N^4 - \frac{1085}{8}N^3 + \frac{8703}{64}N^2 - \frac{9849}{160}N + \frac{363}{40}\right)k^2 + \left(-\frac{73}{80}N^7 + \frac{357}{32}N^6 - \frac{8763}{160}N^5 + \frac{2205}{16}N^4 - \frac{29977}{160}N^3 + \frac{4221}{32}N^2 - \frac{3267}{80}N + \frac{7}{2}\right)k + \left(\frac{1023}{4480}N^8 - \frac{511}{160}N^7 + \frac{1173}{64}N^6 - \frac{889}{16}N^5 + \frac{60921}{640}N^4 - \frac{14539}{160}N^3 + \frac{9801}{224}N^2 - \frac{63}{8}N\right)$$

4) $3N+1 \le k \le 4N$

$$w_k = -\frac{1}{720}k^8 + \left(\frac{3}{80}N - \frac{7}{180}\right)k^7 + \left(-\frac{69}{160}N^2 + \frac{147}{160}N - \frac{161}{360}\right)k^6 + \left(\frac{221}{80}N^3 - \frac{1449}{160}N^2 + \frac{1449}{160}N - \frac{49}{18}\right)k^5 + \left(-\frac{693}{64}N^4 + \frac{1547}{32}N^3 - \frac{4761}{64}N^2 + \frac{735}{16}N - \frac{6769}{720}\right)k^4 + \left(\frac{2141}{80}N^5 - \frac{4851}{32}N^4 + \frac{5083}{16}N^3 - \frac{2415}{8}N^2 + \frac{20307}{160}N - \frac{3283}{180}\right)k^3 + \left(-\frac{6549}{160}N^6 + \frac{44961}{160}N^5 - \frac{47817}{64}N^4 + \frac{7735}{8}N^3 - \frac{200169}{320}N^2 + \frac{29547}{160}N - \frac{363}{20}\right)k^2 + \left(\frac{2843}{80}N^7 - \frac{45843}{160}N^6 + \frac{147729}{160}N^5 - \frac{24255}{16}N^4 + \frac{213707}{160}N^3 - \frac{97083}{160}N^2 + \frac{9801}{80}N - 7\right)k + \left(-\frac{60213}{4480}N^8 + \frac{19901}{160}N^7 - \frac{150627}{320}N^6 + \frac{14987}{16}N^5 - \frac{640131}{640}N^4 + \frac{103649}{160}N^3 - \frac{225423}{1120}N^2 + \frac{198}{8}N\right)$$

5) $4N-3 \le k \le (9N-8)/2$

$$w_k = \frac{1}{567}k^8 + \left(-\frac{1}{16}N + \frac{7}{144}\right)k^7 + \left(\frac{31}{32}N^2 - \frac{49}{32}N + \frac{161}{288}\right)k^6 + \left(-\frac{135}{16}N^3 + \frac{651}{32}N^2 - \frac{483}{32}N + \frac{245}{72}\right)k^5 + \left(\frac{2891}{64}N^4 - \frac{4725}{32}N^3 + \frac{10695}{64}N^2 - \frac{1225}{16}N + \frac{6769}{576}\right)k^4 + \left(-\frac{2439}{16}N^5 + \frac{20237}{32}N^4 - \frac{15525}{16}N^3 + \frac{5425}{8}N^2 - \frac{6769}{32}N + \frac{3283}{144}\right)k^3 + \left(\frac{10159}{32}N^6 - \frac{51219}{32}N^5 + \frac{199479}{64}N^4 - \frac{32625}{8}N^3 + \frac{89931}{64}N^2 - \frac{9849}{32}N + \frac{363}{16}\right)k^2 +$$

$$\left(-\frac{5985}{16}N^7+\frac{71113}{32}N^6-\frac{168291}{32}N^5+\frac{101185}{16}N^4-\frac{130545}{32}N^3+\frac{43617}{32}N^2-\frac{3267}{16}N+\frac{35}{4}\right)k+\left(\frac{857291}{4480}N^8-\frac{41895}{32}N^7+\frac{233657}{64}N^6-\frac{85365}{16}N^5+\frac{2795597}{640}N^4-\frac{63315}{32}N^3+\frac{101277}{224}N^2-\frac{315}{8}N\right)$$